Oblique convergence causes both thrust and strike-slip ruptures during the 2021 M 7.2 Haiti earthquake

Ryo Okuwaki[1,2,3] **& Wenyuan Fan**[4]

[1]Mountain Science Center, University of Tsukuba, Tsukuba, Ibaraki 305-8572, Japan
[2]Faculty of Life and Environmental Sciences, University of Tsukuba, Tsukuba, Ibaraki 305-8572, Japan
[3]COMET, School of Earth and Environment, University of Leeds, Leeds LS2 9JT, UK
[4]Scripps Institution of Oceanography, UC San Diego, La Jolla, California 92093, USA

Key Points:

- The M 7.2 2021 Haiti earthquake sequentially ruptured two disconnected thrust and strike-slip faults
- Neither the thrust or strike-slip fault aligns with the Enriquillo-Plantain Garden fault configuration
- Faulting variability of the earthquake likely reflects the complex deformation partition at the tectonic boundary

Corresponding author: Ryo Okuwaki, rokuwaki@geol.tsukuba.ac.jp

Abstract

A devastating magnitude 7.2 earthquake struck Southern Haiti on 14 August 2021. The earthquake caused severe damage and over 2000 casualties. Resolving the earthquake rupture process can provide critical insights into hazard mitigation. Here we use integrated seismological analyses to obtain the rupture history of the 2021 earthquake. We find the earthquake first broke a blind thrust fault and then jumped to a disconnected strike-slip fault. Neither of the fault configurations aligns with the left-lateral tectonic boundary between the Caribbean and North American plates. The complex multi-fault rupture may result from the oblique plate convergence in the region, so that the initial thrust rupture is due to the boundary-normal compression and the following strike-slip faulting originates from the Gonâve microplate block movement, orienting SW-NE direction. The complex rupture development of the earthquake suggests that the regional deformation is accommodated by a network of segmented faults with diverse faulting conditions.

Plain Language Summary

On 14 August 2021, a devastating magnitude 7.2 earthquake struck Southern Haiti, causing over 2000 casualties and severe infrastructure damage. Southern Haiti situates in between the Caribbean and North American plates, where they converge obliquely at the boundary. The relative motion displaces the plates horizontally and accumulates stress along a major left-lateral fault network. The oblique plate motion also causes an uplift of the region due to the boundary-normal compression. Therefore, earthquakes in the region rupture in complex ways. However, the physical relations between the tectonic regime and the earthquake rupture development are poorly understood, posing challenges to local risk management. Here we use global seismic records to resolve the rupture history of the 2021 Haiti earthquake. We find the earthquake composed of two distinct rupture episodes: a reverse faulting subevent near the epicenter and a strike-slip faulting subevent further west. Both subevents ruptured faults that deviate away from the left-lateral geometry of the Enriquillo-Plantain Garden fault zone. Our results show that the complex tectonic setting of the convergence boundary is imprinted in a segmented fault network with various distinct faulting styles, which may have been influenced by the local small-scale plate fragmentation.

Introduction

Haiti is located in a transpressive tectonic boundary that is seismically active and prone to damaging earthquakes (Manaker et al., 2008; Saint Fleur et al., 2015; Benford et al., 2012) (Fig. 1). The Caribbean plate obliquely converges with the North American plate at 19–20 mm yr^{-1} towards the northeast. The plate motions are largely accommodated by the Septentrional fault zone in the north and the Enriquillo-Plantain Garden fault (EPGF) zone in the south, forming the intermediate Gonâve microplate (Mann et al., 1984; Prentice et al., 2010) (Fig. 1). The oblique convergence results in compressional uplifts in Hispaniola (Haiti and Dominican Republic) in addition to the dominant left-lateral plate movements (Pubellier et al., 2000; Mann et al., 1995). Such a complex tectonic setting drives the development of an intertwined fault system, involving blind secondary faults and segmented faults with various geometries (Jackson et al., 2006; Hayes et al., 2010; Hamling et al., 2017). These faults do not always align with the apparent plate motions and can be missed from geological surveys and geodetic measurements, leading to unexpectedly complex earthquakes, such as the moment magnitude (M_W) 7.0 2010 Haiti earthquake (Hayes et al., 2010; Saint Fleur et al., 2015, 2020).

On 14 August 2021, a devastating M_W 7.2 earthquake struck the Tiburon Peninsula, Haiti, ~96 km west of the 2010 earthquake (Fig. 1). The earthquake caused at least 2000+ casualties and severe infrastructural damage in densely populated areas (reported by the Haitian Civil Protection, Emergency Response Coordination Centre, 2021). The U.S. Geological Survey (USGS) National Earthquake Information Center (NEIC) reported the earthquake origin on 2021-08-14 12:29:08 (UTC) at 18.408°N, 73.475°W, ~125 km west from Port-au-Prince capital city (U.S. Geological Survey Earthquake Hazards Program, 2017). The Global Centroid Moment Tensor (GCMT) solution suggests an oblique strike-slip faulting style of the 2021 Haiti earthquake (Dziewonski et al., 1981; Ekström et al., 2012). The interferometric synthetic aperture radar (InSAR) shows co-seismic uplift near the epicenter and north of EPGF (Geospatial Information Authority of Japan, 2021). The satellite images also suggest westward deformations ~60 km west of the epicenter (Geospatial Information Authority of Japan, 2021). The complex crustal deformation suggests a possible multi-fault rupture of the 2021 Haiti earthquake, with faulting geometries that do not seem to align with the main EPGF configuration (Fig. 1).

We investigate the rupture evolution of the 2021 Haiti earthquake by performing integrated seismological analyses, including teleseismic finite-fault inversion and *P*-wave back-projection. Our methods require minimal assumptions of the earthquake rupture propagation. Here we find the earthquake cascadingly ruptured at least two disconnected faults with different faulting styles. The earthquake initiated on a blind thrust fault and then jumped onto a strike-slip fault propagating westward from the epicenter. The fault geometries of the two rupture episodes do not align with the superficial lineament of EPGF. The initial thrust slip likely released strain accumulated from the EPGF-normal convergence. The second strike-slip subevent likely ruptured a fault plane 45° counterclockwise of the EPGF strike, agreeing with the oblique block motion oriented southwest-northeast. Our source models show that the 2021 earthquake did not rupture the main EPGF but broke secondary faults that were previously

unrecognized. The results highlight that the plate convergence is accommodated by a complex fault network with diverse faulting styles in addition to the main EPGF.

Materials and methods

Imaging earthquake rupture processes is critical to understanding earthquake-source physics and assessing hazards induced by ground shaking. However, it can be challenging when multiple different faults are involved (Hayes et al., 2010; Meng et al., 2012; Ulrich et al., 2019). For example, finite-fault inversion often preassumes a fault plane, which limits identifying hidden earthquake rupture processes of different focal mechanisms. The prior information (assumptions) about the fault system may often be inaccurate and differ from the true rupture faults at depth. Such assumption-induced errors can be significant for remote earthquakes when other geophysical and geological observations are limited. Therefore, exploring seismic records with minimal assumptions is highly desirable for uncovering complex earthquake rupture processes.

To analyze the rupture evolution of the 2021 Haiti earthquake, we use a time-domain back-projection method (Ishii et al., 2005; Fan & Shearer, 2015) and a new finite-fault inversion approach (Yagi & Fukahata, 2011; Shimizu et al., 2020). We take advantage of both low- and high-frequency seismic records of globally distributed networks and arrays. The back-projection method is effective at resolving coherent earthquake high-frequency radiation and can identify possible multiple rupture episodes of large earthquakes across complex fault systems with minimal assumptions (Yao et al., 2011; Meng et al., 2012; Satriano et al., 2012; Nissen et al., 2016; D. Wang et al., 2016; Lay et al., 2018; Kehoe & Kiser, 2020). Therefore, it has been successfully implemented to study the spatiotemporal evolution of complex earthquakes, including multi-fault rupture and supershear rupture earthquakes (e.g., Meng et al., 2012; Fan et al., 2016; Hicks et al., 2020). To resolve the earthquake slip distribution, we apply a finite-fault inversion method that is based on the potency-density tensor approach (Shimizu et al., 2020). We directly resolve the fault geometry by representing the fault slip as the superposition of five-basis double couple components (Kikuchi & Kanamori, 1991) and can obtain a spatiotemporal distribution of the potency density (Ampuero & Dahlen, 2005). The method is particularly suitable for investigating the 2021 Haiti earthquake as it can flexibly accommodate rupture scenarios involving multiple faults with various geometries. Further, the method explicitly introduces an error term of Green's function into the data covariance matrix to account for the associated uncertainties (Yagi & Fukahata, 2011). Such a formulation advances the conventional finite-fault inversion by avoiding modeling errors due to fault geometry assumptions and has proven valuable in resolving complex large earthquakes (Okuwaki et al., 2020; Tadapansawut et al., 2021; Hicks et al., 2020; Yamashita et al., 2021). The obtained slip models have illuminated previously unknown fault geometries and sporadic rupture propagations in geometrically complex fault systems (Tadapansawut et al., 2021; Yamashita et al., 2021). Our integrated strategy of earthquake-source imaging is designed to resolve the rupture evolution without assuming the rupture speed, rupture direction, or fault geometry.

Back-projection

We use vertical-component teleseismic *P* waveforms from globally distributed arrays (839 stations within 30° to 90° epicentral distance) for the back-projection analysis to image the rupture propagation (Fig. S1). We filter the records at 0.2 to 1 Hz with a second-order Butterworth filter. For a data quality-control step, records with signal-to-noise ratios (SNR) less than 5 are removed. The SNR is defined as the root-mean-square (RMS) amplitude ratio from time windows 20 s before and 20 s after the theoretical *P*-wave arrival obtained from IASP91 (B. Kennett & Engdahl, 1991). We further discard stations that are close to the GCMT nodal planes, and the remaining traces are visually examined to assure clear *P* wave onsets. The travel time errors due to the 3D velocity structure are corrected by aligning initial *P* waves with multi-channel cross-correlations of the waveforms within −1 s to 8 s of the theoretical arrivals. We only use records with positive *P*-wave polarities and average cross-correlation coefficients greater than 0.6 to image the earthquake. We grid potential sources at a 10-km horizontal spacing with the grids fixed at the hypocentral depth, covering a 600 km by 600 km area with its epicenter at the center of the grids. Back-projection images are obtained through the *N*th root stacking method (Rost & Thomas, 2002; Xu et al., 2009) with $N = 4$. The *N*th root method can sharpen the back-projection images but would distort the absolute amplitude of the stacks (Rost & Thomas, 2002; Xu et al., 2009). Seismic records are self-normalized and inversely scaled by the number of contributing stations within 5° of each other. Such a procedure can neutralize the radiation pattern effects and balance the spatial coverage of stations. To evaluate the rupture propagation, we compute back-projection snapshots with a 10-second stacking window at a 5-second step for five time windows (Fig. 1). These snapshots are normalized by the maximum power of each window (Fig. 1).

The globally distributed arrays maximize the azimuthal coverage of the earthquake, allowing a high spatial resolution of the back-projected results (Fan & Shearer, 2015). We have considered possible biases from the depth and water phases, but such effects would be minor in our results because the earthquake was shallow and we use a long stacking window, and the results are located far away from the coast (Fan & Shearer, 2015, 2018). The robustness of the back-projection results is quantitatively evaluated by a Jackknife re-sampling exercise (Efron & Tibshirani, 1994; Fan & Shearer, 2016) (Fig. 3). The spatial uncertainties of the peak loci are less than 50 km along latitude and 11 km along longitude (Fig. 1 and 3). The spatial uncertainties along the strike (268° azimuth) show that the station geometry is optimally suited to track the rupture-front migration (Fig. 3).

Finite-fault Inversion

Our finite-fault inversion method is based on a potency-density tensor approach (Shimizu et al., 2020). We use vertical-component teleseismic *P* waveforms from 43 globally distributed stations (Fig. S2). The data are procured to ensure good azimuthal coverage of high-quality records, with signal-to-noise ratios that are sufficient for reliable picks of the *P*-wave first motions (Okuwaki et al., 2016). The first motions are manually determined. The data are then deconvolved from instrument responses into

velocity time series at a 0.6 s sampling interval. To obtain Green's functions, we used the ak135 model (B. L. Kennett et al., 1995) to calculate travel time, ray parameter, and geometric spreading factors. Green's functions are calculated based on a method of the ray-theory approach (Kikuchi & Kanamori, 1991). The CRUST1.0 model (Laske et al., 2013) is used to extract a one-dimensional layered velocity model near the source region to calculate Haskel propagator in Green's functions. We do not apply a low-pass filter to either the observed or synthetic waveforms, and we intend to retrieve detailed rupture processes recorded in the high-frequency components of the seismic records (Shimizu et al., 2020).

Guided by available seismological and geodetic observations (U.S. Geological Survey Earthquake Hazards Program, 2017; Dziewonski et al., 1981; Ekström et al., 2012), we design a planer model domain for the finite-fault inversion (Fig. 1). The model space extends along 268° strike and 64° dip directions based on the GCMT solution (Dziewonski et al., 1981; Ekström et al., 2012), and covers an area of 170-km in length and 35-km in width. To evaluate possible errors that may arise from the model-domain geometry, we also test alternative geometries adopting a 90° or 0° dipping planer domain (Fig. S3) (see Results section). Each sub-fault is separated by 10 km and 5 km along the strike and dip directions, respectively. The slip-rate function for each source grid is represented by linear B-splines at a temporal interval of 0.6 s. The total source duration is set as 30 s. The maximum rupture velocity is set as 5 km/s, which is guided by the back-projection results (Fig. 3). We set the hypocenter at 18.408°N, 73.475°W, and 12-km at depth for the initial rupture point, based on the earthquake origin reported by USGS NEIC (U.S. Geological Survey Earthquake Hazards Program, 2017). After obtaining a preferred finite-fault model, we evaluate the resolvability of the preferred model by using synthetic waveforms from the solution of the 2021 Haiti earthquake (Figs. 1–3) to invert for a new slip model. The results show that the input and output models agree well (Fig. S4), suggesting that the data coverage is sufficient, the inversion is stable, and our obtained finite-fault model of the 2021 Haiti earthquake is robust.

Results

The back-projection images suggest an apparent unilateral westward rupture propagation of the 2021 Haiti earthquake, involving two discrete episodes of strong seismic radiation (0.2–1 Hz). During the first 10 s, we observe the rupture centered near the epicenter with a minor horizontal migration of ~10 km eastward of the epicenter (Fig. 3). Another episode of strong seismic radiation occurs 15 s later and is 60 km westward from the epicenter. The rupture front continued propagating westward till 90 km away from the epicenter lasting for a total of ~30 s (Fig. 1). Intriguingly, there is an apparent spatial gap between the two high-frequency episodes, spanning about 60 km horizontally (Fig. 1). Given that we use a 10 s long stacking time window with a 5 s overlapping time step, this apparent gap is likely real and may represent two distinct subevents. We have tested time windows of various lengths, and this sporadic feature remains the same.

The finite-fault model finds two major slip patches, one centered near the epicenter and the other 70 km west of the epicenter (Fig. 1). The first slip patch is dominated by a reverse faulting mechanism near the epicenter. The resolved focal mechanisms suggest a fault plane striking along the east-west direction with a dipping angle of ~63°. The model domain with the final slip over 1.3 m extends about 40 km by 30 km. This episode of slip released 35% of the total seismic moment for about 10 seconds, centered at a depth of 20 km. The second major slip patch has a vertically dipping, strike-slip faulting mechanism. The dominant strike is 223° or 313°, and the slip area covers an area of 40 km in length and 25 km in width of the model domain. Most slips of the second episode occurred from 12 s to 22 s at a depth shallower than ~20 km, releasing 32% of the total seismic moment. The two major slip patches and their disparate mechanisms are robustly resolved despite different choices of the model domain configuration (Fig. S3). Using either a purely vertical or horizontal dipping planer domain, we obtain very similar slip features as of our preferred finite-fault model (Fig. S3). The stability results from using teleseismic P-waves that our finite-fault inversion approach is insensitive to an assumed spatial model domain (e.g., Shimizu et al., 2020). The total seismic moment of the finite-fault model is 1.3×10^{22} N m (M_W 7.3) for the 2021 Haiti earthquake.

The back-projection and finite-fault models collectively show that the 2021 Haiti earthquake involves at least two discrete rupture episodes, E1 and E2 (Figs. 2 and 3). For the first 10 s of the rupture, the first slip episode (E1) compactly broke a thrust fault within 20 km of the hypocenter. The back-projection images suggest an apparent slow horizontal rupture speed of 1–2 km/s (along 268° azimuth), and the finite-fault model shows that the slip of E1 extends to 25 km at depth. These results suggest that the along dip rupture likely controls this episode. After a temporary hiatus (8 to 12 s) of slip propagation, the second episode (E2) suddenly starts in the western part of the model domain (60 km away from the epicenter, Fig. 3). The horizontal rupture speed of E2 is 4–5 km/s (along 268° azimuth), much faster than that of E1. The moment release starts to decelerate after ~20 s and ceases at ~25 s. Our source models show different faulting styles of E1 and E2 and resolve a clear separation of the two subevents in both space and time.

Discussion

Thrusting faulting of E1 reflecting the oblique plate convergence

The 2021 Haiti earthquake shows a two-stage, multi-segment rupture process involving both thrust and strike-slip faulting styles. The rupture process is unexpected as there is no indication of permitting such a complex evolution from the surface expression of EPGF. The seismic data strongly requires E1 to have a reverse faulting style, a blind thrust fault (Fig. S5). InSAR images show an uplift deformation north of EPGF (Geospatial Information Authority of Japan, 2021) (Fig. S8), and the aftershocks (up to 1 month) also cluster in the northern side of EPGF (Fig. 1). Although it is difficult to identify the fault plane solely from the finite-fault model, multiple lines of geophysical evidence suggest a north-dipping fault plane of E1, striking the east-west direction.

The majority of E1's moment is released at depth. Assuming the earthquake initiated at 12 km depth (close to the USGS origin), the finite-fault model indicates E1 migrating from shallow (12 km) to deep (25 km) for the first 10 s, rupturing downward within a compact region. The downward rupture propagation corroborates the temporal horizontal stagnation of E1 shown in the back-projection results. Such a rupture scenario would explain the subtle surface deformation imaged by InSAR near the epicenter.

The thrust faulting style of E1 contrasts with the left-lateral strike-slip system of EPGF, illuminating a blind fault releasing compressional strains, which is not registered in the Styron et al. (2020) active fault database. Intriguingly, the E1 rupture area coincides with a region with steep topography near the edge of the l'Asile basin, which is filled with Miocene units overlaying the Cretaceous fold units (Wessels et al., 2019). The E1 strike aligns with a high topographic trend of the region along the east-west direction. Additionally, the Global Positioning System (GPS) velocity modeling (Benford et al., 2012; Calais et al., 2016) shows that the oblique plate convergence is partitioned into an EPGF-parallel motion at 8.7 mm yr^{-1} and an EPGF-normal motion at 6.0 mm yr^{-1} (Wessels et al., 2019). Therefore, we speculate that E1 reflects a faulting process that uplifts and shortens the crust in the l'Asile region corresponding to the EPGF-normal compression (Fig. 4). Such a faulting process at an oblique transpressive tectonic boundary would have contributed to the development of this topographic feature, leading to folding and thrusting that have been documented by geological surveys (Wessels et al., 2019).

To the east of the l'Asile basin, there was a destructive earthquake in 1770 near the 2021 Haiti earthquake (Fig. 1), with a rupture process that is poorly constrained (Calais et al., 2010; Bakun et al., 2012). If the 1770 earthquake released most of the accumulated strain, then there would be a slip deficit amounting to ~2 m since the last event. E1 of the 2021 Haiti earthquake only slipped about 0.3 m along the EPGF parallel direction, suggesting the remaining slip deficit may be accommodated by future earthquakes in the l'Asile region.

Strike-slip faulting of E2 deviating away from the main EPGF strand

E2 ruptured a vertical strike-slip fault and lasted for about 13 s (from 12 to 25 s). The E2 strike is likely either at a ~223° (southwest) or ~313° (northwest) azimuth suggested by the finite-fault model. The back-projection images show a southwestward rupture propagation, favoring the ~223° strike-slip fault. This strike direction differs from the major trend of EPGF, oriented at a ~268° azimuth. The inter-seismic GPS velocity fields suggest an obliquely convergent direction along the northeast-southwest direction (~50° azimuth) between the Gonâve microplate and the Caribbean plate (Benford et al., 2012; Calais et al., 2016) (Fig. 4). Such a deformation pattern is inconsistent with the accumulated strain being released purely by strike-slip motion along the EPGF at the ~268° direction, but suggests that part of the elastic strain is partitioned in the EPGF-normal direction.

Given the relative plate motion, it is not surprising that E2 ruptured a fault plane rotated counterclockwise from the EPGF strike to the northeast-southwest direction

(~223° azimuth), and we interpret this to be a direct consequence of the oblique plate convergence. The topographic feature around the 2021 Haiti earthquake transitions from the l'Asile basin (near E1) to the Macaya mountain (near E2, peak elevation 2347 m), which are connected by the Clonard and Camp-Perrin basins (Saint Fleur et al., 2020) (Fig. 4). Within the EPGF system, the fault strike veers counterclockwise from the l'Asile basin to the Camp-Perrin basin. The veering likely formed the left-step of the EPGF at ~74°W, with a pull-apart motion that could have formed the basins. Such a tectonic setting would create faults with various geometries but with limited spatial extent, as the whole fault network is confined within 110 km. The intertwined fault network may rupture at once, leading to complex, sporadic rupture developments, such as the 2021 Haiti earthquake.

We observe a strong seismic radiation episode at the western end of E2 from 20 to 30 s. The finite-fault model shows that the focal mechanisms of this last episode (20–30 s) differ slightly from those of slips at 15 to 20 s (Fig. 3). The 20–30 s slips remain as strike-slip ruptures, but their nodal planes are rotated about ~10° clockwise at a ~233° azimuth (Fig. 3). If this geometric variation holds true, the fault rotation can serve as a restraining bend (Bruhat et al., 2016), which may have caused a sudden deceleration of the rupture and generated stopping phases, radiating strong high-frequency seismic energy (Madariaga, 1977; Bernard & Madariaga, 1984; Spudich & Frazer, 1984; Okuwaki & Yagi, 2018).

Interferometric Synthetic Aperture Radar (InSAR) observations are not included to invert for the earthquake slip distribution as the regional dense vegetation and widely triggered landslides may complicate and hinder InSAR from accurately measuring changes between satellite images (NASA/JPL-Caltech/Copernicus, 2021; Martinez et al., 2021). However, the displacement fields obtained from InSAR can validate finite-fault models. The surface line-of-sight (LOS) displacements of descending and ascending tracks obtained using ALOS-2 (Geospatial Information Authority of Japan, 2021) and Sentinel-1 (NASA/JPL-Caltech/Copernicus, 2021) interferograms show complex patterns and indicate that the earthquake rupture westward from the epicenter (Geospatial Information Authority of Japan, 2021), likely breaking more than one fault (Figs. S8 and S9). Such a spatial pattern agrees well with our back-projection and finite-fault models (Figs. S8 and S9). Both the descending and ascending frames show negative LOS displacements around E1 near the epicenter with a clear east-west lineament edge, indicating uplifts in the north. Near the E2 domain, the surface deformation exceeds 0.8 m in the northern section across EPGF, and a sharp oblique deformation lineament cuts through an EPGF strand near the E2 rupture domain (annotation, Fig. S8b), which likely corresponds to surface ruptures (Geospatial Information Authority of Japan, 2021).

We further forward-model the LOS surface displacements using a suite of finite-fault solutions and compare the model predictions to the observations. In addition to the preferred finite-fault model (E1+E2, Figs. S8g,h and S9g,h), we also examine LOS surface displacements predicted by the USGS finite-fault model (U.S. Geological Survey Earthquake Hazards Program, 2017) (Figs. S8c,d and S9c,d), a model fixing the subfaults as having the GCMT focal mechanism (Dziewonski et al., 1981; Ekström et al., 2012) but with our obtained moments (Figs. S8e,f and S9e,f), a model fixing the E2 strike as that of E1 and keeping the remaining parameters the same as our

preferred finite-fault solution (E1+E1, Figs. S8i,j and S9i,j), and a model fixing the E2 strike as that of EPGF and keeping the remaining parameters the same as our preferred finite-fault solution (E1+EPGF, Figs. S8k,l and S9k,l). The LOS displacements are modeled using the finite-fault models within an elastic half-space (Okada, 1985) assuming a shear modulus of 36 GPa and a Poisson's ratio of 0.25. The predicted LOS displacements using the preferred finite-fault model (E1+E2) can explain the observed uplifts near the hypocenter as due to the reverse faulting of E1 (Figs. S8g,h and S9g,h), and the sharp oblique lineament deformation is predicted by the E2 rupture, which cannot be explained by E1 or hypothesized slips along EPGF (Fig. S8). However, our finite-fault solution does not predict the positive surface deformation north of the E2 domain in the descending frame. This might be due to left-lateral slips along other fault segments, which might have different strikes than E2 or EPGF. Such rupture details would have been missed by the finite-fault model because of the smoothing constraints used to stabilize the inversion. It is also nontrivial to isolate the co-seismic slip from the InSAR images because of the local terrestrial condition and acquisition delays (e.g., 3 and 4 days after the mainshock for the ALOS-2/PALSAR-2 images). The aftershocks and widely triggered landslides (NASA Earth Observatory, 2021; Martinez et al., 2021) might have contributed to the observed surface displacements as well. Overall, the GCMT model cannot explain the descending frame displacements, and the USGS model can explain some surface displacement features albeit missing details. Qualitatively, the preferred finite-fault model (E1+E2) and the model adopting EPGF strike for E2 (E1+EPGF) seem to provide the best fits, yielding similar matches to the observations. In particular, slips along the EPGF strike in the E2 rupture domain could explain certain details better than the resolved E2 strike at some locations. The similar data fit of the two models hampers the hypothesis that E2 strike counterclockwise rotates 45° from the EPGF orientation.

To investigate the E2 strike, we examine Rayleigh-to-Love wave amplitude ratios of broadband seismic stations within 30° epicenteral distance. Rayleigh-to-Love wave amplitude ratio is insensitive to 3D path effects but is highly sensitive to earthquake radiation pattern (focal mechanism). Therefore, the spatial pattern of Rayleigh-to-Love wave amplitude ratio can independently evaluate the fault configurations. We first download three-component, broadband seismic data at a total of 77 stations spanning all azimuths. The data are filtered at a 20–50 s period band with a 4th-order Butterworth bandpass filter. We then rotate the horizontal components to measure and compute Rayleigh-to-Love wave amplitude ratios at each station. The observed Rayleigh-to-Love wave amplitude ratios agree well the predicted ones from our preferred finite-fault model (E1+E2, Fig. S10) for stations at most azimuths. We find that our preferred finite-fault model provides the best fit to the observed amplitude ratios and the E2 strike rotating 45° from the EPGF orientation is necessary to explain the stations in northeastern US. Other source models, including the GCMT and E1+EPGF models, cannot explain the observed amplitude ratios (Dziewonski et al., 1981; Ekström et al., 2012) (Fig. S10). The validation exercises using independent datasets collectively favor that the focal mechanism of E2 differs from that of E1 and the E2 strike likely rotates 45° counterclockwise from the EPGF orientation.

Strong motion records and local geodetic datasets would provide additional constraints to the 2021 earthquake rupture properties. However, most of such datasets are unavailable at the moment, limiting their use to resolve the rupture process. For example, only one seismic station (AY.NQUSE) near Port-au-Prince (AY.NQUSE station) has reported the earthquake records to IRIS, and the nearest GNSS station (JME2) is located ~100 km away from the epicenter. The data scarcity prohibits further analyses using near-field data to resolve the Haiti earthquake. Our rupture models might help to guide future investigations when the data are publicly available.

Complex fault network and its implication for hazard risks

Disconnected faults can interact and trigger each other in various ways during either a single event or an earthquake sequence (Harris et al., 1991, 2002; Nissen et al., 2016; Ruppert et al., 2018; Freed, 2005; Fan & Shearer, 2016; Goldberg et al., 2020). The E1 and E2 fault segments are separated by ~60 km and ruptured sequentially within 10 s (Fig. 1), leading to an apparent migration speed of ~6 km/s, which is comparable to the local *P*-wave velocity in Southern Haiti (Douilly et al., 2013, 2016). In conjunction with possible minor effects from static Coulomb stress changes (see Text S1 for details), such a spatiotemporal relation during the 2021 Haiti earthquake indicates that the discontinuous jump from E1 to E2 may have been caused by the dynamic effects from the passing seismic waves.

The 2021 Haiti earthquake locates ~96 km apart from the 2010 Haiti earthquake, and both earthquakes involve blind thrust faults in a similar fashion (Hayes et al., 2010). The correlation raises the question of whether the 2010 earthquake triggered the 2021 Haiti earthquake. Such an earthquake-to-earthquake triggering process has been reported at various tectonic settings, and the 1992 Landers earthquake and the 1999 Hector Mine earthquake in southern California resemble a similar pair to the Haiti earthquakes (e.g., Parsons & Dreger, 2000; Felzer et al., 2002; Pollitz & Sacks, 2002). Both the Landers and Hector Mine earthquakes are strike-slip events involving multiple segments with similar magnitudes of the Haiti earthquakes, and the Landers earthquake likely triggered the Hector Mine earthquake after eight years with static stress changes likely involved in its nucleation (e.g., Pollitz & Sacks, 2002; Price & Burgmann, 2002; Zeng, 2001). Although unraveling such stress interactions between the 2010 and 2021 Haiti earthquakes will require more detailed analysis, our preliminary Coulomb stress analyses suggests that the static stress changes on the E1 fault induced by the 2010 Haiti earthquake (Hayes et al., 2010) are minor at a 12 km depth as low as <10 kPa (see Text S1 for details). Future analyses using near-field observations may offer insights in the inter-connections between the two M7 Haiti earthquakes.

The different focal mechanisms of E1 and E2 suggest that the 2021 Haiti earthquake likely ruptured a disconnected fault networks. Multi-fault earthquakes often cause more high frequency radiations than single-fault earthquakes. For example, slip migrating between different faults would cause abrupt change of rupture velocity and/or slip rate, and such geometric complexities would cause more high-frequency radiations (Aki, 1979; Madariaga et al., 2006; Kase & Day, 2006; Okuwaki & Yagi, 2018). Further, irregular fault structures and misaligned complex fault networks can inter-

act with each other during earthquake ruptures, impacting earthquake rupture dynamics by producing intense high-frequency ground motions (e.g., Tsai & Hirth, 2020; Tsai et al., 2021; Chu et al., 2021). Therefore, earthquakes rupturing complex fault networks would likely produce stronger high-frequency ground motions, imposing greater hazard risks. Resolving such complex multi-fault rupture processes will offer physical insights into possible rupture scenarios and aid future hazard assessment.

Conclusions

We identify two distinct rupture episodes of the M_W 7.2 2021 Haiti earthquake. In the first episode, E1 ruptured a blind thrust fault, and the earthquake then jumped to a strike-slip fault (E2) that is 60 km west of the epicenter. The complex rupture process likely results from the regional oblique plate convergence. The second subevent strikes at a direction differing from the EPGF network trend. Its southwest-northeast strike orientation reflects the oblique convergence motion between the Caribbean plate and the Gonâve microplate. The discontinuous jump from E1 to E2 ruptures is likely facilitated by dynamic triggering. The complex tectonic setting produces multiple-segmented fault patches that have various focal mechanisms, and the 2021 Haiti earthquake exemplifies that these fault patches may rupture at once, causing devastating hazards over a large region.

Open Research

All the materials presented in this paper are archived and available at https://doi.org/10.5281/zenodo.5534984. The seismic data were downloaded through the IRIS Wilber 3 system (https://ds.iris.edu/wilber3/find_event) or IRIS Web Services (https://service.iris.edu). We used ObsPy (https://doi.org/10.5281/zenodo.165135; Beyreuther et al., 2010), Pyrocko (https://pyrocko.org/; The Pyrocko Developers, 2017), matplotlib (https://doi.org/10.5281/zenodo.592536; Hunter, 2007), Generic Mapping Tools (https://doi.org/10.5281/zenodo.3407865; Wessel & Luis, 2017); and Scientific colour maps (https://doi.org/10.5281/zenodo.1243862; Crameri, 2018; Crameri et al., 2020) for data processing and visualization.

Acknowledgments

We thank editor Germán Prieto, associate editor Victor Tsai, and two anonymous reviewers for their evaluations and constructive suggestions. The facilities of IRIS Data Services, and specifically the IRIS Data Management Center, were used for access to waveforms, related metadata, and/or derived products used in this study. IRIS Data Services are funded through the Seismological Facilities for the Advancement of Geoscience (SAGE) Award of the National Science Foundation under Cooperative Support Agreement EAR-1851048. The authors declare no conflicts of interest relevant to this study. W.F. acknowledges support from NSF grant EAR-2022441. We thank Tim J. Wright for fruitful discussions. We thank Yu Morishita, Hiroshi Munekane, and Masaki Kuwahara at Geospatial Information Authority of Japan for providing their ALOS-2/PALSAR-2 interferograms.

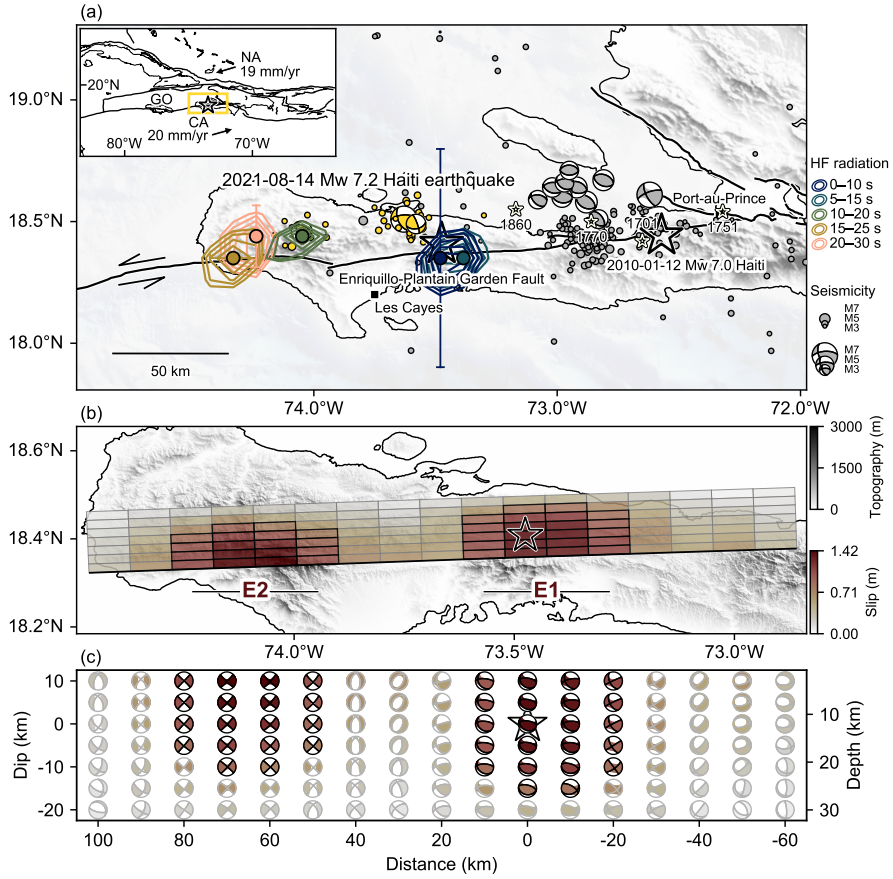

Figure 1. Finite-fault and back-projection models of the 2021 Haiti earthquake and seismotectonic summary of the Tiburon Peninsula, Southern Haiti. (a) The colored contours show the back-projection results. The location uncertainties (one standard deviation of latitude or longitude) are from Jackknife re-sampling. The black stars show the epicenters of the 2021 and 2010 Haiti earthquakes (U.S. Geological Survey Earthquake Hazards Program, 2017). The white stars show historical earthquakes in the region (Bakun et al., 2012). The gray dots are the background seismicity, and the yellow dots are the 1-month aftershocks of the 2021 Haiti earthquake. The gray and yellow beach balls show available GCMT solutions of the events (Dziewonski et al., 1981; Ekström et al., 2012) before and after the 2021 Haiti earthquake. The black lines show active faults in the region (Styron et al., 2020). The inset shows regional tectonics (yellow rectangle, Fig. 1a) with the black lines as the plate boundaries (Bird, 2003) and the arrow showing the relative plate velocity vector between the Caribbean (CA) and the North American (NA) plates (DeMets et al., 2010) juxtaposed against the Gonâve (GO) microplate. The star shows the epicenter of the 2021 Haiti earthquake. The topography/bathymetry is from GEBCO Bathymetric Compilation Group 2019 (2019). (b) The colored cells show the finite-fault solution. Large slip patches (>50% of the maximum slip) are empathized by black cell boarders. The topography is from Shuttle Radar Topography Mission (U.S. Geological Survey, 2015). (c) The cross-section of the moment-tensor distribution extracted from the resultant potency-density tensors. All the beach balls of the moment-tensor solution are represented as a lower-hemisphere stereographic projection (far-side focal sphere). The solution with large slip (>50% of the maximum slip) is empathized by black line.

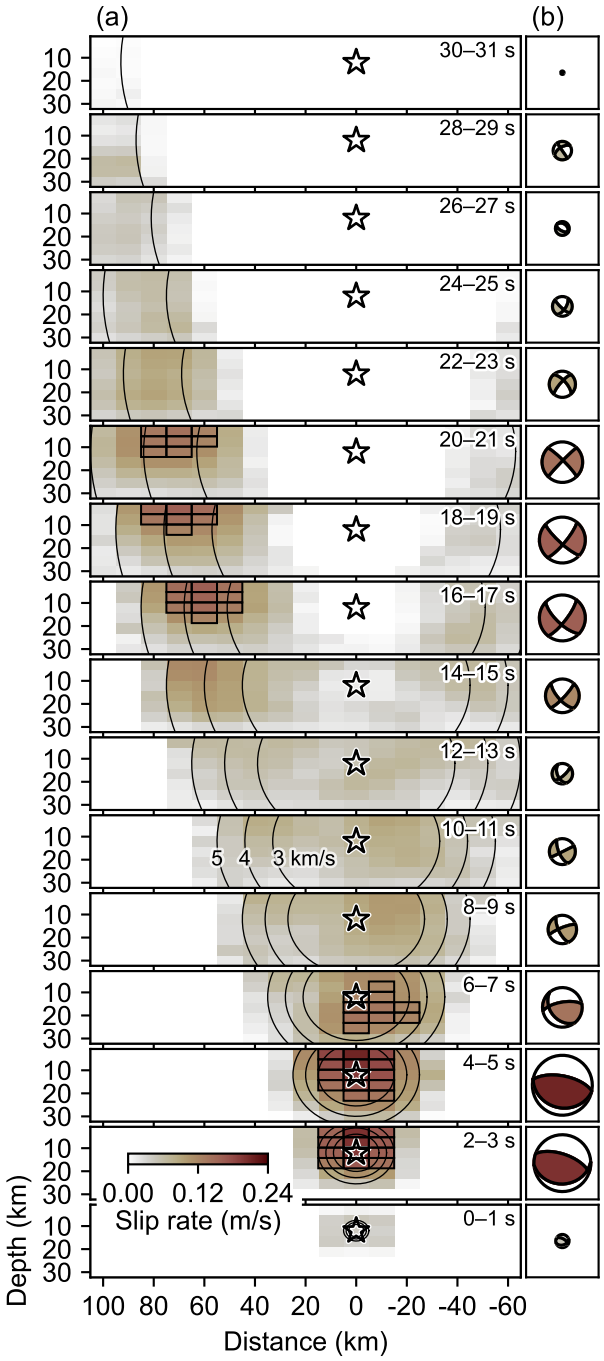

Figure 2. Snapshots of the finite-fault model. (a) The cross section of the slip-rate distribution. Large slip rate areas (>50% of the maximum slip rate) are outlined by the black cell boarders. The star denotes the hypocenter. The black circles are the reference rupture speeds. (b) Centroid moment tensor solutions of the finite-fault model for the snapshot time windows. The color and size of the focal mechanisms correlate with the maximum slip rates of the time windows.

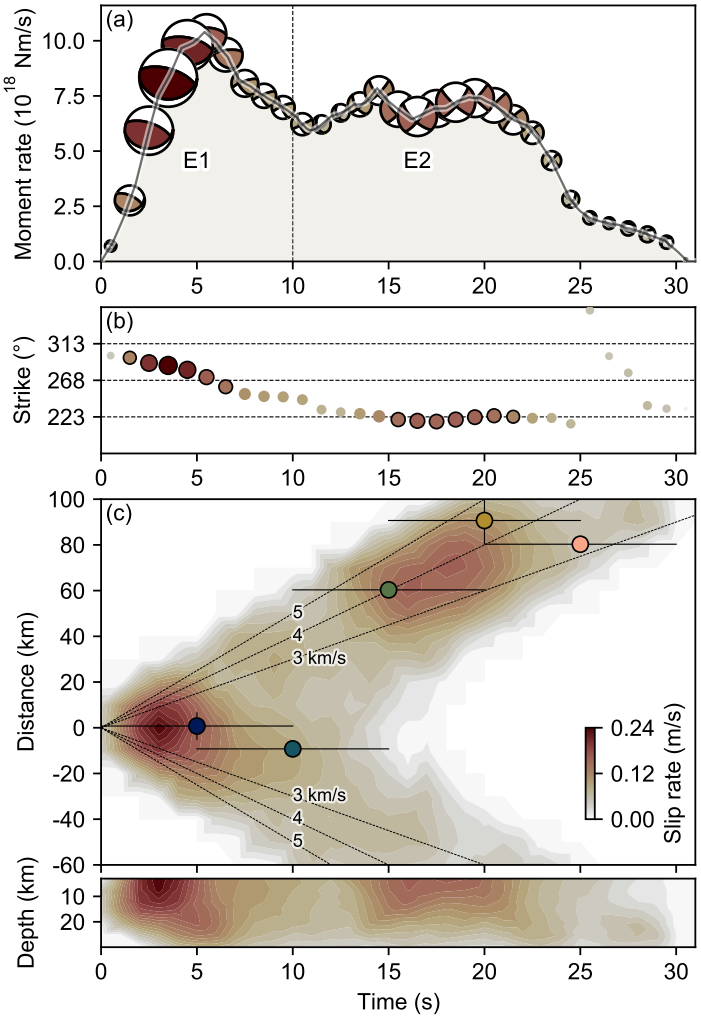

Figure 3. Spatiotemporal evolutions of the finite-fault and back-projection models. (a) Moment rate function of the finite-fault model. The beach balls show the centroid moment tensor solutions of the finite-fault model for the snapshot time windows at every 1 s. The color and size of the focal mechanisms correlate with the maximum slip rates of the time windows. (b) Strikes of the centroid moment tensor solutions shown in Fig. 3a. As reasoned in the paper, we prefer a north-dipping fault plane for E1 from 0–10 s and a southwest-northeast fault plane for E2 from 15–25 s. The color and size of the circles correlate with the maximum slip rates of the time windows with large slip rate snapshots (>50% of the maximum slip rate) outlined by black circles. (c) Spatiotemporal distribution of the finite-fault model and the back-projection peak loci of the five 10-s long windows. The results are projected along a direction of 268° azimuth (middle panel) and along depth (bottom panel, back-projection has no depth resolution for this case). The contours show the slip rate distributions. The colored dots are the back-projection peak loci of the 10-s long snapshots (Fig. 1). The vertical bars are the uncertainty estimates from the jackknife re-sampling exercise and the horizontal bars show the stacking window length. The black lines show the reference rupture speeds.

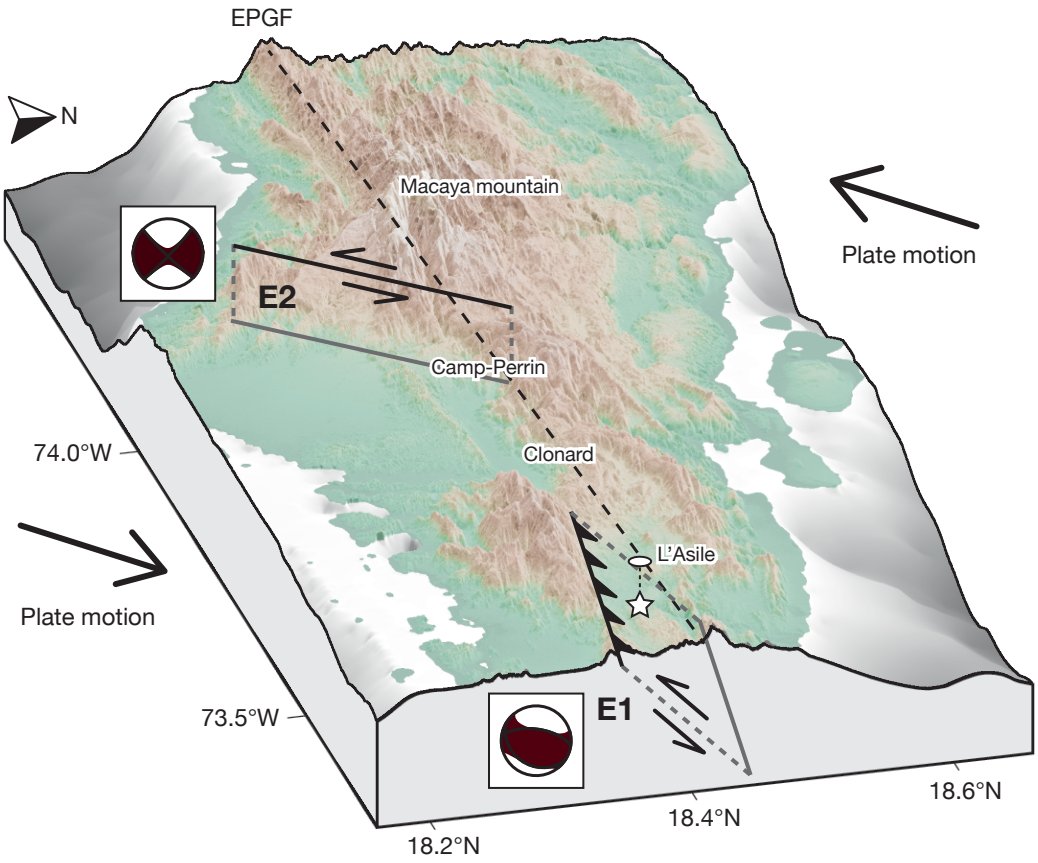

Figure 4. Cartoon interpretation of the faulting process and the cascading rupture development of the 2021 Haiti earthquake. The star shows the hypocenter (U.S. Geological Survey Earthquake Hazards Program, 2017). The one-side arrows show the interpreted fault motions. The beach balls are the centroid moment tensor solutions of the two rupture episodes (E1 and E2, Fig. 1). The solid black lines show the surface projections of faults. The dashed line shows the EPGF trace (268° azimuth). The full arrows show the relative plate motion direction of the Caribbean and Gonâve plates (Benford et al., 2012). The topography is from Shuttle Radar Topography Mission (U.S. Geological Survey, 2015).

References

Aki, K. (1979). Characterization of barriers on an earthquake fault. *J. Geophys. Res.*, *84*(B11), 6140. Retrieved from http://dx.doi.org/10.1029/JB084iB11p06140{%}5Cnhttp://doi.wiley.com/10.1029/JB084iB11p06140http://doi.wiley.com/10.1029/JB084iB11p06140 doi:10.1029/JB084iB11p06140

Ampuero, J.-P., & Dahlen, F. A. (2005). Ambiguity of the Moment Tensor. *Bull. Seism. Soc. Am.*, *95*(2), 390. doi:10.1785/0120040103

Bakun, W. H., Flores, C. H., & ten Brink, U. S. (2012). Significant earthquakes on the Enriquillo fault system, Hispaniola, 1500-2010: Implications for seismic hazard. *Bull. Seismol. Soc. Am.*, *102*(1), 18–30. doi:10.1785/0120110077

Benford, B., Demets, C., & Calais, E. (2012). GPS estimates of microplate motions, northern Caribbean: Evidence for a Hispaniola microplate and implications for earthquake hazard. *Geophys. J. Int.*, *191*(2), 481–490. doi:10.1111/j.1365-246X.2012.05662.x

Bernard, P., & Madariaga, R. (1984). A new asymptotic method for the modeling of near-field accelerograms. *Bull. Seismol. Soc. Am.*, *74*(2), 539–557. doi:10.1785/bssa0740020539

Beyreuther, M., Barsch, R., Krischer, L., Megies, T., Behr, Y., & Wassermann, J. (2010). ObsPy: A Python Toolbox for Seismology. *Seismol. Res. Lett.*, *81*(3), 530–533. doi:10.1785/gssrl.81.3.530

Bird, P. (2003). An updated digital model of plate boundaries. *Geochemistry, Geophys. Geosystems*, *4*(3), 1105. doi:10.1029/2001GC000252

Bruhat, L., Fang, Z., & Dunham, E. M. (2016). Rupture complexity and the supershear transition on rough faults. *J. Geophys. Res. Solid Earth*, *121*(1), 210–224. doi:10.1002/2015JB012512

Calais, E., Freed, A., Mattioli, G., Amelung, F., Jónsson, S., Jansma, P., … Momplaisir, R. (2010). Transpressional rupture of an unmapped fault during the 2010 Haiti earthquake. *Nat. Geosci.*, *3*(11), 794–799. doi:10.1038/ngeo992

Calais, E., Symithe, S., Mercier de Lépinay, B., & Prépetit, C. (2016). Plate boundary segmentation in the northeastern Caribbean from geodetic measurements and Neogene geological observations. *Comptes Rendus - Geosci.*, *348*(1), 42–51. doi:10.1016/j.crte.2015.10.007

Chu, S. X., Tsai, V. C., Trugman, D. T., & Hirth, G. (2021). Fault Interactions Enhance High-Frequency Earthquake Radiation. *Geophys. Res. Lett.*, *48*(20), 1–10. Retrieved from https://onlinelibrary.wiley.com/doi/10.1029/2021GL095271 doi:10.1029/2021GL095271

Crameri, F. (2018). Geodynamic diagnostics, scientific visualisation and StagLab 3.0. *Geosci. Model Dev.*, *11*(6), 2541–2562. doi:10.5194/gmd-11-2541-2018

Crameri, F., Shephard, G. E., & Heron, P. J. (2020). The misuse of colour in science communication. *Nat. Commun.*, *11*(1), 5444. doi:10.1038/s41467-020-19160-7

DeMets, C., Gordon, R. G., & Argus, D. F. (2010). Geologically current plate motions. *Geophys. J. Int.*, *181*(1), 1–80. doi:10.1111/j.1365-246X.2009.04491.x

Douilly, R., Ellsworth, W. L., Kissling, E., Freed, A. M., Deschamps, A., & Mercier de Lépinay, B. (2016). 3-D velocity structure in southern Haiti from local

earthquake tomography. *J. Geophys. Res. Solid Earth*, *121*(12), 8813–8832. doi:10.1002/2016JB013123

Douilly, R., Haase, J. S., Ellsworth, W. L., Bouin, M. P., Calais, E., Symithe, S. J., ... Hough, S. E. (2013). Crustal structure and fault geometry of the 2010 Haiti earthquake from temporary seismometer deployments. *Bull. Seismol. Soc. Am.*, *103*(4), 2305–2325. doi:10.1785/0120120303

Dziewonski, A. M., & Anderson, D. L. (1981). Preliminary reference Earth model. *Phys. Earth Planet. Inter.*, *25*(4), 297–356. Retrieved from http://www.sciencedirect.com/science/article/pii/0031920181900467https://linkinghub.elsevier.com/retrieve/pii/0031920181900467 doi:10.1016/0031-9201(81)90046-7

Dziewonski, A. M., Chou, T.-A., & Woodhouse, J. H. (1981). Determination of earthquake source parameters from waveform data for studies of global and regional seismicity. *J. Geophys. Res. Solid Earth*, *86*(B4), 2825–2852. doi:10.1029/JB086iB04p02825

Efron, B., & Tibshirani, R. (1994). *An Introduction to the Bootstrap*. doi:10.1201/9780429246593

Ekström, G., Nettles, M., & Dziewoński, A. (2012). The global CMT project 2004–2010: Centroid-moment tensors for 13,017 earthquakes. *Phys. Earth Planet. Inter.*, *200-201*, 1–9. doi:10.1016/j.pepi.2012.04.002

Emergency Response Coordination Centre. (2021). *Haiti - Earthquake, update (DG ECHO, GDACS, Copernicus EMS, Haiti Civil Protection).* (https://erccportal.jrc.ec.europa.eu/ECHO-Products/Echo-Flash#/echo-flash-items/21504)

Fan, W., & Shearer, P. M. (2015). Detailed rupture imaging of the 25 April 2015 Nepal earthquake using teleseismic P waves. *Geophys. Res. Lett.*, *42*(14), 5744–5752. doi:10.1002/2015GL064587

Fan, W., & Shearer, P. M. (2016). Local near instantaneously dynamically triggered aftershocks of large earthquakes. *Science*, *353*(6304), 1133–1136. doi:10.1126/science.aag0013

Fan, W., & Shearer, P. M. (2018). Coherent seismic arrivals in the P wave coda of the 2012 Mw 7.2 Sumatra earthquake: Water reverberations or an early aftershock? *J. Geophys. Res. Solid Earth*, *123*(4), 3147–3159. doi:10.1002/2018JB015573

Fan, W., Shearer, P. M., Ji, C., & Bassett, D. (2016). Multiple branching rupture of the 2009 Tonga-Samoa earthquake. *J. Geophys. Res. Solid Earth*, *121*(8), 5809–5827. doi:10.1002/2016JB012945

Felzer, K. R., Becker, T. W., Abercrombie, R. E., Ekström, G., & Rice, J. R. (2002). Triggering of the 1999 Mw 7.1 Hector Mine earthquake by aftershocks of the 1992 Mw 7.3 Landers earthquake. *J. Geophys. Res. Solid Earth*, *107*(B9), ESE–6. doi:10.1029/2001JB000911

Freed, A. M. (2005). Earthquake triggering by static, dynamic, and post-seismic stress transfer. *Annu. Rev. Earth Planet. Sci.*, *33*(1), 335–367. doi:10.1146/annurev.earth.33.092203.122505

GEBCO Bathymetric Compilation Group 2019. (2019). *The GEBCO_2019 Grid - a continuous terrain model of the global oceans and land.* British Oceanographic Data Centre, National Oceanography Centre, NERC, UK. doi:10/c33m

Geospatial Information Authority of Japan. (2021). *The 2021 Haiti Earthquake: Crustal deformation detected by ALOS-2 data.* (https://www.gsi.go.jp/cais/topic20210814-e.html)

Goldberg, D. E., Melgar, D., Sahakian, V., Thomas, A., Xu, X., Crowell, B., & Geng, J. (2020). Complex rupture of an immature fault zone: A simultaneous kinematic model of the 2019 Ridgecrest, CA earthquakes. *Geophysical Research Letters*, *47*(3), e2019GL086382. doi:10.1029/2019GL086382

Hamling, I. J., Hreinsdóttir, S., Clark, K., Elliott, J., Liang, C., Fielding, E., ... Stirling, M. (2017). Complex multifault rupture during the 2016 Mw 7.8 Kaikōura earthquake, New Zealand. *Science*, *356*(6334). doi:10.1126/science.aam7194

Harris, R. A., Archuleta, R. J., & Day, S. M. (1991). Fault steps and the dynamic rupture process: 2-D numerical simulations of a spontaneously propagating shear fracture. *Geophys. Res. Lett.*, *18*(5), 893–896. doi:10.1029/91GL01061

Harris, R. A., Dolan, J. F., Hartleb, R., & Day, S. M. (2002). The 1999 İzmit, Turkey, earthquake: A 3D dynamic stress transfer model of intraearthquake triggering. *Bull. Seismol. Soc. Am.*, *92*(1), 245–255. doi:10.1785/0120000825

Hayes, G. P., Briggs, R. W., Sladen, A., Fielding, E. J., Prentice, C., Hudnut, K., ... Simons, M. (2010). Complex rupture during the 12 January 2010 Haiti earthquake. *Nat. Geosci.*, *3*(11), 800–805. doi:10.1038/ngeo977

Hicks, S. P., Okuwaki, R., Steinberg, A., Rychert, C. A., Harmon, N., Abercrombie, R. E., ... Sudhaus, H. (2020). Back-propagating supershear rupture in the 2016 Mw 7.1 Romanche transform fault earthquake. *Nat. Geosci.*, *13*(9), 647–653. doi:10.1038/s41561-020-0619-9

Hunter, J. D. (2007). Matplotlib: A 2D Graphics Environment. *Comput. Sci. Eng.*, *9*(3), 90–95. doi:10.1109/MCSE.2007.55

Ishii, M., Shearer, P. M., Houston, H., & Vidale, J. E. (2005). Extent, duration and speed of the 2004 Sumatra-Andaman earthquake imaged by the Hi-Net array. *Nature*, *435*(7044), 933–936. doi:10.1038/nature03675

Jackson, J., Bouchon, M., Fielding, E., Funning, G., Ghorashi, M., Hatzfeld, D., ... Wright, T. (2006). Seismotectonic, rupture process, and earthquake-hazard aspects of the 2003 December 26 Bam, Iran, earthquake. *Geophys. J. Int.*, *166*(3), 1270–1292. doi:10.1111/j.1365-246X.2006.03056.x

Kase, Y., & Day, S. M. (2006). Spontaneous rupture processes on a bending fault. *Geophys. Res. Lett.*, *33*(10), 1–4. Retrieved from http://doi.wiley.com/10.1029/2006GL025870 doi:10.1029/2006GL025870

Kehoe, H., & Kiser, E. (2020). Evidence of a supershear transition across a fault stepover. *Geophys. Res. Lett.*, *47*(10), e2020GL087400. doi:10.1029/2020GL087400

Kennett, B., & Engdahl, E. (1991). Traveltimes for global earthquake location and phase identification. *Geophys. J. Int.*, *105*(2), 429–465. doi:10.1111/j.1365-246X.1991.tb06724.x

Kennett, B. L., Engdahl, E. R., & Buland, R. (1995). Constraints on seismic velocities in the Earth from traveltimes. *Geophys. J. Int.*, *122*(1), 108–124. doi:10.1111/j.1365-246X.1995.tb03540.x

Kikuchi, M., & Kanamori, H. (1991). Inversion of complex body waves-III. *Bull. Seism. Soc. Am.*, *81*(6), 2335–2350. doi:10.1785/BSSA0810062335

King, G. C., Stein, R. S., & Lin, J. (1994). Static stress changes and the triggering of earthquakes. *Bull. Seismol. Soc. Am.*, *84*(3), 935–953. doi:10.1785/BSSA0840030935

Krischer, L., Hutko, A. R., van Driel, M., Stähler, S., Bahavar, M., Trabant, C., & Nissen-Meyer, T. (2017). On-Demand Custom Broadband Synthetic Seismograms. *Seismol. Res. Lett.*, *88*(4), 1127–1140. Retrieved from https://doi.org/10.1785/0220160210https://pubs.geoscienceworld.org/srl/article/88/4/1127-1140/354100 doi:10.1785/0220160210

Laske, G., Masters, T. G., Ma, Z., & Pasyanos, M. (2013). Update on CRUST1.0 - A 1-degree Global Model of Earth's Crust. *Geophys. Res. Abstr. 15*, *Abstr. EGU2013-2658*, *15*, Abstract EGU2013–2658. (https://igppweb.ucsd.edu/~gabi/crust1.html)

Lay, T., Ye, L., Bai, Y., Cheung, K. F., & Kanamori, H. (2018). The 2018 MW 7.9 Gulf of Alaska Earthquake: Multiple Fault Rupture in the Pacific Plate. *Geophys. Res. Lett.*, *45*(18), 9542–9551. doi:10.1029/2018GL079813

Lin, J., & Stein, R. S. (2004). Stress triggering in thrust and subduction earthquakes and stress interaction between the southern San Andreas and nearby thrust and strike-slip faults. *J. Geophys. Res. Solid Earth*, *109*(B2), 1–19. doi:10.1029/2003jb002607

Madariaga, R. (1977). High-frequency radiation from crack (stress drop) models of earthquake faulting. *Geophys. J. Int.*, *51*(3), 625–651. doi:10.1111/j.1365-246X.1977.tb04211.x

Madariaga, R., Ampuero, J. P., & Adda-Bedia, M. (2006). *Seismic Radiation from Simple Models of Earthquakes.* Retrieved from https://doi.org/10.1029/170GM23 doi:https://doi.org/10.1029/170GM23

Mai, P. M., & Thingbaijam, K. K. (2014). SRCMOD: An online database of finite-fault rupture models. *Seismol. Res. Lett.*, *85*(6), 1348–1357. doi:10.1785/0220140077

Manaker, D. M., Calais, E., Freed, A. M., Ali, S. T., Przybylski, P., Mattioli, G., ... De Chabalier, J. B. (2008). Interseismic plate coupling and strain partitioning in the Northeastern Caribbean. *Geophys. J. Int.*, *174*(3), 889–903. doi:10.1111/j.1365-246X.2008.03819.x

Mann, P., Burke, K., & Matumoto, T. (1984). Neotectonics of Hispaniola: plate motion, sedimentation, and seismicity at a restraining bend. *Earth Planet. Sci. Lett.*, *70*(2), 311–324. doi:10.1016/0012-821X(84)90016-5

Mann, P., Taylor, F. W., Edwards, R. L., & Ku, T. L. (1995). Actively evolving microplate formation by oblique collision and sideways motion along strike-slip faults: An example from the northeastern Caribbean plate margin. *Tectonophysics*, *246*(1-3), 1–69. doi:10.1016/0040-1951(94)00268-E

Martinez, S. N., Allstadt, K. E., Slaughter, S. L., Schmitt, R. G., Collins, E., Schaefer, L. N., & Ellison, S. (2021). *Landslides triggered by the August 14, 2021, magnitude 7.2 Nippes, Haiti, earthquake* (Tech. Rep.). Reston, VA. Retrieved from http://pubs.er.usgs.gov/publication/ofr20211112 doi:10.3133/ofr20211112

Meng, L., Ampuero, J. P., Stock, J., Duputel, Z., Luo, Y., & Tsai, V. C. (2012). Earthquake in a maze: Compressional rupture branching during the 2012 Mw 8.6 Sumatra earthquake. *Science*, *337*(6095), 724–726.

doi:10.1126/science.1224030

NASA Earth Observatory. (2021). *Earthquake in Haiti Triggers Landslides.* Retrieved from https://earthobservatory.nasa.gov/images/148713/earthquake-in-haiti-triggers-landslides (https://earthobservatory.nasa.gov/images/148713/earthquake-in-haiti-triggers-landslides)

NASA/JPL-Caltech/Copernicus. (2021). *Satellite Data Shows Ground Motion from August 2021 Haiti Earthquake.* Retrieved from https://www.jpl.nasa.gov/images/pia23697-satellite-data-shows-ground-motion-from-august-2021-haiti-earthquake (https://www.jpl.nasa.gov/images/pia23697-satellite-data-shows-ground-motion-from-august-2021-haiti-earthquake, https://aria-share.jpl.nasa.gov/20210814-Haiti_EQ/Displacements/)

Nissen, E., Elliott, J. R., Sloan, R. A., Craig, T. J., Funning, G. J., Hutko, A., ... Wright, T. J. (2016). Limitations of rupture forecasting exposed by instantaneously triggered earthquake doublet. *Nat. Geosci.*, *9*(4), 330–336. doi:10.1038/ngeo2653

Nissen-Meyer, T., van Driel, M., Stähler, S. C., Hosseini, K., Hempel, S., Auer, L., ... Fournier, A. (2014). AxiSEM: broadband 3-D seismic wavefields in axisymmetric media. *Solid Earth*, *5*(1), 425–445. Retrieved from https://se.copernicus.org/articles/5/425/2014/ doi:10.5194/se-5-425-2014

Okada, Y. (1985). Surface deformation due to shear and tensile faults in a half-space. *Bull. Seismol. Soc. Am.*, *75*(4), 1135–1154. Retrieved from https://doi.org/10.1785/BSSA0750041135 doi:10.1785/BSSA0750041135

Okuwaki, R., Hirano, S., Yagi, Y., & Shimizu, K. (2020). Inchworm-like source evolution through a geometrically complex fault fueled persistent supershear rupture during the 2018 Palu Indonesia earthquake. *Earth Planet. Sci. Lett.*, *547*, 116449. doi:10.1016/j.epsl.2020.116449

Okuwaki, R., & Yagi, Y. (2018). Role of geometric barriers in irregular-rupture evolution during the 2008 Wenchuan earthquake. *Geophys. J. Int.*, *212*(3), 1657–1664. doi:10.1093/gji/ggx502

Okuwaki, R., Yagi, Y., Aránguiz, R., González, J., & González, G. (2016). Rupture Process During the 2015 Illapel, Chile Earthquake: Zigzag-Along-Dip Rupture Episodes. *Pure Appl. Geophys.*, *173*(4), 1011–1020. doi:10.1007/s00024-016-1271-6

Parsons, T., & Dreger, D. S. (2000). Static-stress impact of the 1992 Landers earthquake sequence on nucleation and slip at the site of the 1999 m 7.1 Hector Mine earthquake, southern California. *Geophys. Res. Lett.*, *27*(13), 1949–1952. doi:10.1029/1999GL011272

Pollitz, F. F., & Sacks, I. S. (2002). Stress triggering of the 1999 Hector Mine earthquake by transient deformation following the 1992 Landers earthquake. *Bull. Seismol. Soc. Am.*, *92*(4), 1487–1496. doi:10.1785/0120000918

Prentice, C. S., Mann, P., Crone, A. J., Gold, R. D., Hudnut, K. W., Briggs, R. W., ... Jean, P. (2010). Seismic hazard of the Enriquillog-Plantain Garden fault in Haiti inferred from palaeoseismology. *Nat. Geosci.*, *3*(11), 789–793. doi:10.1038/ngeo991

Price, E. J., & Burgmann, R. (2002). Interactions between the Landers and Hector Mine, California, earthquakes from space geodesy, boundary element model-

ing, and time-dependent friction. *Bull. Seismol. Soc. Am.*, *92*(4), 1450–1469. doi:10.1785/0120000924

Pubellier, M., Mauffret, A., Leroy, S., Vila, J. M., & Amilcar, H. (2000). Plate boundary readjustment in oblique convergence: Example of the neogene of hispaniola, Greater Antilles. *Tectonics*, *19*(4), 630–648. doi:10.1029/2000TC900007

Rost, S., & Thomas, C. (2002). Array seismology: Methods and applications. *Rev. Geophys.*, *40*(3), 1008. doi:10.1029/2000RG000100

Ruppert, N. A., Rollins, C., Zhang, A., Meng, L., Holtkamp, S. G., West, M. E., & Freymueller, J. T. (2018). Complex Faulting and Triggered Rupture During the 2018 MW 7.9 Offshore Kodiak, Alaska, Earthquake. *Geophys. Res. Lett.*, *45*(15), 7533–7541. doi:10.1029/2018GL078931

Saint Fleur, N., Feuillet, N., Grandin, R., Jacques, E., Weil-Accardo, J., & Klinger, Y. (2015). Seismotectonics of southern Haiti: A new faulting model for the 12 January 2010 M7.0 earthquake. *Geophys. Res. Lett.*, *42*(23), 10273–10281. doi:10.1002/2015GL065505

Saint Fleur, N., Klinger, Y., & Feuillet, N. (2020). Detailed map, displacement, paleoseismology, and segmentation of the Enriquillo-Plantain Garden Fault in Haiti. *Tectonophysics*, *778*, 228368. doi:10.1016/j.tecto.2020.228368

Satriano, C., Kiraly, E., Bernard, P., & Vilotte, J.-P. (2012). The 2012 Mw 8.6 Sumatra earthquake: Evidence of westward sequential seismic ruptures associated to the reactivation of a N-S ocean fabric. *Geophys. Res. Lett.*, *39*(15). doi:10.1029/2012GL052387

Shimizu, K., Yagi, Y., Okuwaki, R., & Fukahata, Y. (2020). Development of an inversion method to extract information on fault geometry from teleseismic data. *Geophys. J. Int.*, *220*(2), 1055–1065. doi:10.1093/gji/ggz496

Spudich, P., & Frazer, L. N. (1984). Use of ray theory to calculate high-frequency radiation from earthquake sources having spatially variable rupture velocity and stress drop. *Bull. Seismol. Soc. Am.*, *74*(6), 2061–2082. doi:10.1785/BSSA0740062061

Styron, R., García-Pelaez, J., & Pagani, M. (2020). CCAF-DB: The Caribbean and Central American active fault database. *Nat. Hazards Earth Syst. Sci.*, *20*(3), 831–857. doi:10.5194/nhess-20-831-2020

Tadapansawut, T., Okuwaki, R., Yagi, Y., & Yamashita, S. (2021). Rupture Process of the 2020 Caribbean Earthquake Along the Oriente Transform Fault, Involving Supershear Rupture and Geometric Complexity of Fault. *Geophys. Res. Lett.*, *48*(1), 1–9. doi:10.1029/2020GL090899

The Pyrocko Developers. (2017). *Pyrocko: A Versatile Seismology Toolkit for Python.* doi:10.5880/GFZ.2.1.2017.001

Toda, S., Stein, R. S., Richards-Dinger, K., & Bozkurt, S. B. (2005). Forecasting the evolution of seismicity in southern California: Animations built on earthquake stress transfer. *J. Geophys. Res. Solid Earth*, *110*(5), 1–17. doi:10.1029/2004JB003415

Tsai, V. C., & Hirth, G. (2020). Elastic Impact Consequences for High-Frequency Earthquake Ground Motion. *Geophys. Res. Lett.*, *47*(5), 1–8. Retrieved from https://onlinelibrary.wiley.com/doi/10.1029/2019GL086302 doi:10.1029/2019GL086302

Tsai, V. C., Hirth, G., Trugman, D. T., & Chu, S. X. (2021). Impact Versus Frictional Earthquake Models for High-Frequency Radiation in Complex Fault Zones. *J. Geophys. Res. Solid Earth*, *126*(8), 1–17. Retrieved from https://onlinelibrary.wiley.com/doi/10.1029/2021JB022313 doi:10.1029/2021JB022313

Ulrich, T., Vater, S., Madden, E. H., Behrens, J., van Dinther, Y., van Zelst, I., ... Gabriel, A. A. (2019). Coupled, Physics-Based Modeling Reveals Earthquake Displacements are Critical to the 2018 Palu, Sulawesi Tsunami. *Pure Appl. Geophys.*, *176*(10), 4069–4109. doi:10.1007/s00024-019-02290-5

U.S. Geological Survey. (2015). *Shuttle Radar Topography Mission 1 Arc-Second Global.* doi:10.5066/F7PR7TFT

U.S. Geological Survey Earthquake Hazards Program. (2017). *Advanced National Seismic System (ANSS) Comprehensive Catalog of Earthquake Events and Products.* doi:10.5066/F7MS3QZH

van Driel, M., Krischer, L., Stähler, S. C., Hosseini, K., & Nissen-Meyer, T. (2015). Instaseis: instant global seismograms based on a broadband waveform database. *Solid Earth*, *6*(2), 701–717. Retrieved from https://se.copernicus.org/articles/6/701/2015/ doi:10.5194/se-6-701-2015

Wang, D., Mori, J., & Koketsu, K. (2016). Fast rupture propagation for large strike-slip earthquakes. *Earth Planet. Sci. Lett.*, *440*, 115–126. doi:10.1016/j.epsl.2016.02.022

Wang, J., Xu, C., Freymueller, J. T., Wen, Y., & Xiao, Z. (2021). AutoCoulomb: An automated configurable program to calculate coulomb stress changes on receiver faults with any orientation and its application to the 2020 Mw7.8 Simeonof Island, Alaska, Earthquake. *Seismol. Res. Lett.*, *92*(4), 2591–2609. doi:10.1785/0220200283

Wessel, P., & Luis, J. F. (2017). The GMT/MATLAB Toolbox. *Geochemistry, Geophys. Geosystems*, *18*(2), 811–823. doi:10.1002/2016GC006723

Wessels, R. J., Ellouz-Zimmermann, N., Bellahsen, N., Hamon, Y., Rosenberg, C., Deschamps, R., ... Leroy, S. (2019). Polyphase tectonic history of the Southern Peninsula, Haiti: from folding-and-thrusting to transpressive strike-slip. *Tectonophysics*, *751*, 125–149. doi:10.1016/j.tecto.2018.12.011

Xu, Y., Koper, K. D., Sufri, O., Zhu, L., & Hutko, A. R. (2009). Rupture imaging of the Mw 7.9 12 May 2008 Wenchuan earthquake from back projection of teleseismic P waves. *Geochemistry, Geophys. Geosystems*, *10*(4), Q04006. doi:10.1029/2008GC002335

Yagi, Y., & Fukahata, Y. (2011). Introduction of uncertainty of Green's function into waveform inversion for seismic source processes. *Geophys. J. Int.*, *186*(2), 711–720. doi:10.1111/j.1365-246X.2011.05043.x

Yamashita, S., Yagi, Y., Okuwaki, R., Shimizu, K., Agata, R., & Fukahata, Y. (2021). Consecutive ruptures on a complex conjugate fault system during the 2018 Gulf of Alaska earthquake. *Sci. Rep.*, *11*(1), 5979. doi:10.1038/s41598-021-85522-w

Yao, H., Gerstoft, P., Shearer, P. M., & Mecklenbräuker, C. (2011). Compressive sensing of the Tohoku-Oki Mw 9.0 earthquake: Frequency-dependent rupture modes. *Geophys. Res. Lett.*, *38*(20). doi:10.1029/2011GL049223

Zeng, Y. (2001). Viscoelastic stress-triggering of the 1999 Hector Mine earthquake

799 by the 1992 Landers earthquake. *Geophys. Res. Lett., 28*(15), 3007–3010.
800 doi:10.1029/2000GL012806